

Probing Cosmology with the X-ray Forest

Taotao Fang AND Claude R.Canizares

Department of Physics and Center for Space Research

Massachusetts Institute of Technology

Room 37-624D, 70 Vassar Street, Cambridge, MA 02139

`fangt@space.mit.edu`, `crc@space.mit.edu`

Received _____; accepted _____

ABSTRACT

There is a growing consensus that in the present universe most baryons reside in galaxy clusters and groups in the form of highly ionized gas at temperatures of $10^6 \sim 10^8$ K. The H-like and He-like ions of the heavy elements can produce absorption features - the so-called “X-ray Forest” - in the X-ray spectrum of a background quasar. We investigate the distribution of the X-ray absorption lines produced by this gas under three different cosmological models: the standard CDM with $\Omega_0 = 1$, a flat model with $\Omega_0 = 0.3$ and an open model with $\Omega_0 = 0.3$. We give a semi-analytic calculation of the X-ray forest distribution based on the Press-Schechter formalism, following Perna & Loeb (1998). We choose three ions (O VIII, Si XIV and Fe XXV) and calculate the distribution functions, the number of absorbers along the line-of-sight (LOS) to a distant quasar vs. redshift and column density in a given ion. We find that significant differences in the evolution of the distribution functions among the three cosmological models. Using Monte Carlo simulations, we simulate the distribution of X-ray absorption lines for 10,000 random LOS. We find there are at least several O VIII lines with column density higher than 10^{16}cm^{-2} . Finally we explore the possibility of detecting the X-ray forest with current and upcoming X-ray missions and we present an *XMM* RGS simulation of a representative quasar X-ray spectrum.

Subject headings: galaxies: clusters: general — intergalactic medium — large-scale structure of universe — quasars: absorption lines — X-rays : general

1. Introduction

There is an apparent deficit in the total density of baryons at moderate and low redshift, z , which has come to be called the “missing baryon” problem (see, e.g., Fukugita, Hogan & Peebles 1998; Cen & Ostriker 1999). Observations of the hydrogen and helium absorption lines in the Lyman alpha forest give a baryon density at high redshift ($z \sim 3$) of $\Omega_b \geq 0.017h^{-2}$ (Rauch et al. 1998), which is consistent with the value $\Omega_b = 0.019h^{-2}$ derived from standard big bang nucleosynthesis (Burles & Tytler 1998, a Hubble constant of $H_0 = 100h \text{ km s}^{-1} \text{ Mpc}^{-1}$ is used throughout the paper). However, in the local universe the baryon budget is far below this number. Summing over all the baryons inside stars, neutral atomic gas and molecular gas gives $\Omega_b \sim 0.003h^{-1}$.

There is a growing consensus that these “missing baryons” reside in a hot ($\geq 10^6$ K), ionized plasma associated with groups of galaxies. This is effectively attributing to the universe a mix of components similar to that observed in richer groups and galaxy clusters (Fukugita et al. 1998; Cen & Ostriker 1999). It is plausible that this medium can be enriched in heavy elements. These heavy elements would not be fully ionized at the temperatures of interest, as is the cluster gas (Renzini 1997).

Resonant absorption by a hot, enriched medium would introduce features in the X-ray spectrum of a distant quasar. The features would be narrow lines or broad troughs depending on the velocity structure of the absorber. The associated absorption edges would also be present but are generally much weaker (Markevitch 1999). Early work by Shapiro & Bahcall (1980) discusses the X-ray absorption spectrum introduced by a uniformly distributed, hot IGM with an admixture of metal atoms via X-ray “Gunn-Peterson” effect. Using the same method but with a photoionized model of the IGM, Aldcroft et al. (1994) constrain the density and temperature of the IGM with *ROSAT* PSPC spectra of $z \sim 3$ quasars. Basko, Komberg & Moskalenko (1981) discusses the detectability of X-ray

resonance absorption lines in quasar spectra produced by hot plasma in an intervening galaxy cluster. More detailed and accurate calculations of cluster absorption were performed by Gil’fanov, Syunyaev & Churazov (1987); Krolik & Raymond (1988); Sarazin (1989).

Like the Lyman alpha forest system in the optical band, the spatial distribution of the galaxy groups and clusters can also produce an “X-ray forest” along the line of sight in the X-ray spectrum of a background quasar. The concept of an “X-ray forest” was first suggested by Hellsten, Gnedin & Miralda-Escudé (1998): X-ray absorption lines are produced by hot intergalactic medium in the form of “filamentary and sheet-like structures connected to galaxy clusters and groups, as well as colder gas left out in voids.” A similar concept was explored by Perna & Loeb (1998) using the expected spectrum of mass concentrations for a universe dominated by cold dark matter. The effect of differing cosmologies on the number and evolution of X-ray absorption lines is related to the effect on the number density of clusters (Bahcall & Fan 1998; Eke et al. 1998). This means that X-ray absorption line studies might eventually provide independent constraints on cosmological parameters.

Here we build on and extend the approach of (Perna & Loeb 1998) to explore the X-ray forest for various cosmologies and to assess its detectability. Detecting it is not easy. Most of the absorption lines will have equivalent widths ≤ 1 eV, and none of the previous X-ray missions (*Einstein*, *ASCA*, *ROSAT*) had sufficient sensitivity to detect such features in a quasar spectrum. However, current and future missions give order-of-magnitude advances in sensitivity for the X-ray forest. For example, *Chandra* grating spectrometers have resolving powers of 1,000 around 1 keV (ASC Science Center 1997) with sufficient collecting area to detect an absorption line from an ion column density of approximately 10^{16}cm^{-2} in a plausible quasar spectrum. Assuming a moderate metal abundance, this column density implies a hydrogen column density of a modest galaxy cluster (Canizares & Fang 1998).

XMM and *Constellation-X* achieve comparable or better energy resolutions with larger effective area. In this paper we use simulations to assess the ability of these missions to detect features in the X-ray forest.

This paper is organized as follows: section II gives a semi-analytic calculation of the X-ray forest distribution function, based on Press-Schechter formalism. Section III is devoted to the numerical simulation of the distribution function. In section IV we discuss the detectability of the X-ray forest. Section V presents the conclusions and discussion.

2. X-ray Forest Distribution Function

2.1. Press-Schechter Formalism

Galaxies, galaxy clusters and other large scale structures grow from the initial small scale density fluctuation via gravitational instability. The small scale fluctuation first grows linearly, until it reaches a critical density. Then it decouples from the Hubble expansion, starts collapsing and finally condenses out as a virialized, gravitational bound halo. Given a random Gaussian distribution, the comoving number density of virialized halos can be described by the Press-Schechter function :

$$\frac{dn}{dM_{vir}} = \left(\frac{2}{\pi}\right)^{\frac{1}{2}} \frac{\bar{\rho}}{M_{vir}^2} \frac{\delta_c}{\sigma(z, M_{vir})} \left| \frac{d \ln \sigma}{d \ln M_{vir}} \right| \exp \left(-\frac{\delta_c^2}{2\sigma(z, M_{vir})^2} \right) \quad (1)$$

Here M_{vir} is the mass of the virialized halo; $\bar{\rho} \equiv 3\Omega_0 H_0^2 / 8\pi G$ is the comoving mean density of the universe which is constant during matter domination; δ_c denotes the linearly extrapolated overdensity at which an object virializes; and $\sigma(z, M_{vir})$ is the rms density fluctuation inside halos containing a mean mass of M_{vir} . Press & Schechter (1974) first gave this function with a very simple and intuitive model : large scale virialized objects form from the nonlinear interaction of small scale objects through a self-similar condensation process. However, the original theory suffers the so-called “cloud-in-cloud” problem of

miscounting the underdense regions properly. Bond et al. (1991) and Lacey & Cole (1993) extended this model by counting the overdense regions one-by-one and gave the correct normalization of the mass function. Although no direct observational evidence shows that the Press-Schechter function is the right way to describe the cluster abundance, this function fits N-body simulations extremely well (Lacey & Cole 1994; Eke, Cole & Frenk 1996; Tormen 1998; Frenk et al. 1999).

Formally one would expect δ_c to depend on the cosmological model and the geometry of the collapsing object. Since most of the rich clusters are fairly round it would be a good assumption that the collapse is close to spherical. In a flat universe spherical collapse gives $\delta_c = 1.686$ (Lacey & Cole 1993). However, the value of δ_c changes by $\leq 5\%$ as one goes from an Einstein-de Sitter universe to an $\Omega = 0.1$ universe (Eke, Cole & Frenk 1996). So we adopt the value of 1.686 throughout the paper.

The rms mass variance at redshift z can be expressed by the present rms mass variance and the linear growth factor $D(z)$ through

$$\sigma(z, M) = \sigma(z = 0, M) \frac{D(z)}{D(z = 0)} \quad (2)$$

From observations of cluster density in the local universe, several papers give the normalization of the power spectrum at $8h^{-1}\text{Mpc}$ scale (Eke, Cole & Frenk 1996; Viana & Liddle 1996; Pen 1998; Viana & Liddle 1999). Here we adopt the value from Eke, Cole & Frenk (1996). The present rms mass fluctuation $\sigma(z = 0, M)$ can be calculated by the normalized power spectrum. A functional fit to $D(z)$ is given by Lahav et al. (1991)

To apply the Press-Schechter formalism we need to determine the virial mass of clusters (M_{vir}) precisely. However, measuring the virial mass of clusters is difficult, especially at high redshift. Observationally the X-ray temperature (T_X) of galaxy clusters can be measured more accurately. Numerical simulations and observations of X-ray clusters show that there exists a very tight relationship between T_X and M_{vir} (Hjorth, Oukbir & Kampen

1998; Bryan & Norman 1998). To simply we assume a singular isothermal sphere model of the cluster mass density distribution. The mass-temperature relationship is given by Eke, Cole & Frenk (1996)

$$kT_X = \frac{1.39}{\beta} \left(\frac{M_{vir}}{10^{15} h^{-1} M_\odot} \right)^{\frac{2}{3}} (1+z) \left(\Delta_c \frac{\Omega_0}{\Omega(z)} \right)^{\frac{1}{3}} \text{ keV} \quad (3)$$

Here Δ_c is the ratio of the mean cluster density to the critical density at that redshift, β is the ratio of the specific kinetic energy to thermal energy, Ω_0 and $\Omega(z)$ are the cosmology density parameter at present and redshift of z , respectively.

Recently various authors show that equation (3) is accurately obeyed in N-body hydrodynamic simulations with value of $\beta \simeq 1$ (Navarro, Frenk & White 1995; Evrard, Metzler & Navarro 1996; Bryan & Norman 1998). Although all of them suggest a slightly higher β -value, it might be due to the incomplete thermalization of the intracluster gas, or the gas density dropping faster than r^{-2} around the virial radius in the numerical simulations. Here we use $\beta = 1$, which means that the specific galaxy kinetic energy equals the specific gas thermal energy within the virial radius. A Recent analysis on Abell 401 shows the cluster mass given by the best-fit model is approximately by a factor of 1.7 lower than the value predicted by equation (3) (Nevalainen, Markevitch & Forman 1999). The difference is attributed to the fact that the simulated clusters have steeper gas density and shallower temperature profiles than observed.

2.2. Gas Column Density Profile within Galaxy Clusters

Assuming a “ β model” of the cluster gas density distribution (Sarazin 1988), the column density of gas particles at an impact distance of b is (Perna & Loeb 1998)

$$N_{gas}(b) = \frac{f_{gas} kT_X}{2Gr_c(\mu m_p)^2} \left[1 + \left(\frac{b}{r_c} \right)^2 \right]^{-\frac{1}{2}} \quad (4)$$

Here b is the projected distance from the center of the galaxy cluster; r_c is the core radius of the galaxy cluster and we select a constant value of 250 kpc throughout the paper; f_{gas} is the baryonic gas fraction; $\mu = 0.59$ is the mean atomic weight and k is the Boltzmann constant.

We are interested in the metal ion column density which would produced absorption features in the X-ray spectrum of a background quasar. The ionization sources of intracluster gas can be either photoionization from the X-ray background radiation or collisional ionization. However the X-ray background is in general too weak to be the main source of ionization so we only consider collisional ionization here. Since generally the collisional time scale is much shorter than Hubble time, the gas is in collisional ionization equilibrium. If we denote $\Upsilon(X^i) \equiv N(X^i)/N(X)$ as the fraction of ion X^i , Υ would be only a function of temperature, i.e., $\Upsilon = \Upsilon(T)$ under collisional equilibrium (Sarazin & Bahcall 1977). Assuming a uniform metallicity $Z(X) \equiv N(X)/N(H)$ the ion X^i column density distribution is

$$N(X^i) = 0.46 Z(X) \Upsilon(T) \frac{f_{gas} k T_X}{2 G r_c (\mu m_p)^2} \left[1 + \left(\frac{b}{r_c} \right)^2 \right]^{-\frac{1}{2}} \quad (5)$$

Here 0.46 is the fraction of hydrogen atoms by number.

The baryonic gas fraction within galaxy clusters has recently received attention (White et al. 1993; White & Fabian 1995). Almost all the observations give large values of baryon density Ω_b than expected from the theory of the big bang nucleosynthesis if $\Omega_0 = 1$, which is taken as an indication of a low density universe. Both local and high redshift observations (Rines et al. 1999; Ettori & Fabian 1999) suggest f_{gas} scatters between 0.1 and 0.3. To simplify, we use $f_{gas} = 0.2$ throughout the paper.

2.3. Distribution Function

In analogy to the Lyman- α forest system, we define $\partial^2 P / \partial N^i \partial z$ as the number of absorption systems along the line of sight with a column density between N^i and $N^i + dN^i$ per unit redshift. Here $N^i = N(X^i)$ is the column density of ion X^i . If we define Σ as the cross section of a galaxy group or cluster, the distribution function is then

$$\frac{\partial^2 P}{\partial N^i \partial z} = \int_{T_X} dT_X \frac{dn}{dT_X} \frac{d\Sigma}{dN^i} \frac{d\ell}{dz} \quad (6)$$

Here dn/dT_X is the cluster number density distribution at different cluster temperatures, which can be obtained by the Press-Schechter function and the cluster mass-to-temperature relationship. ℓ is the path length. We refer to Perna & Loeb (1998) for detailed calculations.

3. Computed Distribution

3.1. the X-ray Forest in Different Cosmological Models

Given different cosmological models, the X-ray forest distribution $\partial^2 P / \partial N^i \partial z$ is determined through equation (6) via the Press-Schechter function (equation (1)). Here we compare the X-ray forest distribution under three cosmological models: a standard cold dark matter model (SCDM); a low-density open CDM model (OCDM) and a low-density Λ -dominated CDM model. Table 1 shows all the model parameters.

EDITOR: PLACE TABLE 1 HERE.

Observationally resonance absorption lines will be produced by transitions with the ions of the most abundant elements with the largest oscillator strength. For specificity we choose the ions O VIII, Si XIV and Fe XXV. Table 2 gives all the parameters. Mushotzky et al. (1996) measured the metal abundances in four rich clusters with ASCA. We adopt

their metallicity because we concentrate only on high column densities produced by rich clusters. The redshift evolution of cluster metallicities can also play an important role here, for simplicity we treat them as constants. We adopt the solar abundances from Anders & Grevesse (1989). The atomic data are from Verner, Verner & Ferland (1996). Figure 1 shows the ionization fractions (Mazzotta et al. 1998), in which O VIII, Si XIV and Fe XXV show three different peak temperatures around 2×10^6 , 10^7 and 5×10^7 , respectively. These temperatures roughly correspond to the galaxy cluster mass around $10^{12}M_{\odot}$, $10^{13}M_{\odot}$ and $10^{14}M_{\odot}$, according to the mass-temperature relationship (3).

EDITOR: PLACE TABLE 2 HERE.

EDITOR: PLACE FIGURE 1 HERE.

To compute the Press-Schechter function we use the codes based on Eisenstein & Hu (1998) for the calculation of power spectrum and mass variance $\sigma(M)$. However, their codes are normalized by COBE data, which is on a scale larger than the size of galaxy clusters, so we renormalize the power spectrum based on the observations of the cluster abundance in the local universe.

Figure 2 through figure 4 give the distribution of three elements: Fe XXV, Si XIV and O VIII under three cosmological models at different redshifts. The most striking feature is that in all three ions, the standard cold dark model shows a more rapid evolution than the two other low-density models. This trend in general agrees with the evolutionary scenarios predicted by different cosmological models. In the SCDM model, the density perturbation grows as $(1+z)^{-1}$, most clusters are formed recently and the cluster number density declines very quickly as we move to high redshift. On the other hand, low-density models predict slower evolution. Figure 5 shows the comoving cluster abundances as a function of X-ray

temperature at different redshift predicted by the Press-Schechter distribution. Although LCDM also shows some decline of cluster abundances at high temperature, SCDM show the strongest evolution of number density at temperatures $\geq 5 \times 10^6$ K. Among all three ions, the distribution of Fe XXV shows the biggest decline (over three decades between $z = 0$ and $z = 3$). The reason is that Fe XXV has the highest peak temperature ($\sim 5 \times 10^7$ K) in figure 1, which corresponds to the biggest decline in the cluster abundances (figure 5).

EDITOR: PLACE FIGURE 2 HERE.

EDITOR: PLACE FIGURE 3 HERE.

EDITOR: PLACE FIGURE 4 HERE.

EDITOR: PLACE FIGURE 5 HERE.

The second feature is that all three distributions show a rapid cutoff between 10^{16}cm^{-2} and 10^{17}cm^{-2} . This is mainly because the maximum ion column density can not exceed the central column density of the galaxy clusters. The central ion column density is given by equation (5). For instance, the peak temperature of O VIII is around $2.4 \times 10^6\text{K}$ (figure 1), which roughly corresponds to a central O VIII column density of $6 \times 10^{16}\text{cm}^{-2}$. This explains why figure 4 shows a sharp cutoff around this column density.

The third feature is that for all three ions, the SCDM model predicts more absorbers along the line-of-sight than OCDM and LCDM. This is because the spatial density of clusters is very sensitive to the present matter density - Ω_0 (equation (1)). Ω_0 represents the overall amplitude of the density fluctuation and changing of Ω_0 will dramatically change the spatial density of virialized objects, the clusters of galaxies. This can be a method to determine Ω_0 in the future from observations of the X-ray forest.

3.2. Monte Carlo Simulations

To obtain statistics on the distribution of X-ray absorption lines, we carry out a series of Monte Carlo simulations. Assuming both absorber column density and redshift are independent random variables (Møller & Jakobsen 1990), we define the Probability Density Functions (PDF) for each variable,

$$\begin{aligned} f(z) &= \frac{1}{A} \int_{N_{\min}^i}^{N_{\max}^i} \frac{\partial^2 P}{\partial N^i \partial z} dN^i \\ g(N^i) &= \frac{1}{A} \int_{z_{\min}}^{z_{\max}} \frac{\partial^2 P}{\partial N^i \partial z} dz \end{aligned} \quad (7)$$

Here A is the total absorber number, given by the integration of the distribution function over both redshift and ion column density. We set a range for each variable as $N^i \in [10^{12}, 10^{17}] \text{ cm}^{-2}$ and $z \in [0, 3]$. Using these PDFs we obtain column densities and redshifts for 10,000 randomly selected lines-of-sight. Figures 6 and 7 show the average cumulative distribution of the absorption line numbers vs. column density and redshift, respectively. Although Fe XXV is too scarce to give any statistical information, both figures do reflect the three features of the X-ray forest we noted before. In figure 7 we include only the absorption lines with column density higher than 10^{15} cm^{-2} because this is the lowest column density which is detectable by *Constellation X* (see the next section). In this figure we see that, compared to the LCDM and OCDM models, SCDM presents a larger number of absorption lines. For instance, SCDM shows that on average ten O VIII absorption lines up to $z = 1$, where OCDM and LCDM give only four and three lines, respectively.

EDITOR: PLACE FIGURE 6 HERE.

EDITOR: PLACE FIGURE 7 HERE.

Assuming a velocity dispersion of $b \sim 300 \text{ km sec}^{-1}$, the line optical depth is obtained by $\tau(\nu) = N^i \sigma(\nu)$. Here $\sigma(\nu)$ is the absorption cross section at frequency ν (Spitzer 1978). The line-of-sight transmission is defined as $D \equiv e^{-\tau}$. Figures 8 to 10 show the transmission of Fe XXV, Si XIX and O VIII under the three cosmological models, to $z = 3$.

EDITOR: PLACE FIGURE 8 HERE.

EDITOR: PLACE FIGURE 9 HERE.

EDITOR: PLACE FIGURE 10 HERE.

4. Detectability

Generally most X-ray absorption lines we discuss here are narrow, unresolved lines. For a weak absorption line, the equivalent width W_{eq} is given by (Spitzer 1978)

$$\frac{W_{eq}}{E} = \frac{b}{c} \int_{-\infty}^{+\infty} \left\{ 1 - \exp \left(-\tau_0 e^{-x^2} \right) \right\} dx \quad (8)$$

Where E is the line energy, b and c are velocity dispersion and light speed. Here τ_0 is the optical depth at line center, $\tau_0 \equiv N s \lambda / \pi^{1/2} b$, where N is ion column density, λ is wavelength and s is the Einstein absorption coefficient.

The detectability of the X-ray forest is limited by the spectral resolving power and effective area of the spectrometer. A weak, unresolved resonance line has $W_{eq} \ll \Delta E$, where ΔE is the bin width, determined by the instrument resolving power R ($R \equiv E/\Delta E$). Suppose we use an instrument with resolving power R to observe an resonance line around

energy E (keV). The source spectrum has a continuum intensity of F_X (in units of photons $\text{cm}^{-2} \text{s}^{-1} \text{keV}^{-1}$) around E . Given an observing time T , the minimum detectable equivalent width for an unresolved absorption line is

$$W_{eq} \gtrsim (S/N) \left(\frac{E}{A_{eff} \cdot R \cdot F_X \cdot T} \right)^{\frac{1}{2}} \quad (9)$$

Here (S/N) is the signal-to-noise ratio and A_{eff} is the effective area, and we assume negligible background.

For illustration we choose a typical spectrum of an X-ray bright quasar with photon index $\Gamma = 2.5$ and flux $1.0 \times 10^{-11} \text{ ergs cm}^{-2}\text{sec}^{-1}$ between 0.1 and 2.4 keV. The Galactic column density is $5.0 \times 10^{20} \text{ cm}^{-2}$. Given this representative spectrum we calculate the minimum detectable equivalent width and column density of some ion species for a particular observation time. In Table 3, we list three instruments: *Chandra* LETG/HETG, *XMM* RGS and *Constellation-X* Calorimeter/Gratings. Assuming the absorption ions are located at $z = 0.5$, the equivalent width is calculated based on a S/N of 3 and an integration time of 100 ksec. Comparing this table with figure 6 and 7, we find that O VIII ion is the best candidate for all three instruments. Using XSPEC 10, we simulate this “representative” spectrum plus O VIII absorption lines from one realization of the LCDM model (Figure 10) on *XMM* RGS. Several tens of quasars with $z \geq 1$ have such spectrum or are even brighter, so we put the redshift of this quasar at $z = 1$. The LCDM simulations give three absorption lines with $z \leq 1$ and $N \geq 10^{16} \text{ cm}^{-2}$. Table 4 lists the simulated line properties. Then we fit the simulated spectrum with a model only containing Galactic absorption and a single power law. The χ^2 plot of figure 11 clearly shows three absorption lines. Notice here line 2 and line 3 are only separated by approximately 3.7 eV.

EDITOR: PLACE TABLE 3 HERE.

EDITOR: PLACE TABLE 4 HERE.

EDITOR: PLACE FIGURE 11 HERE.

5. Summary

In this paper we use a semi-analytic method to investigate the X-ray forest. Following previous work (Perna & Loeb 1998) we calculate the X-ray distribution function of O VIII, Si XIV and Fe XXV under the Standard cold dark matter model and two low-density models. Fe XXV shows the more rapid evolution of SCDM, compared to OCDM and LCDM; These trends are milder for Si XIV and O VIII. Using Monte-Carlo simulation, we investigate the average distribution of the X-ray forest. We find SCDM model presents more absorption lines than OCDM and LCDM, which eventually might yield a method of determining Ω_0 . We also select a typical spectrum of an X-ray bright, distant quasar to explore the detectability of the X-ray forest. We find for all three telescopes, there are at least several O VIII absorption lines detectable by *Chandra*, *XMM* and *Constellation-X*. This result is consistent with Perna & Loeb (1998) and Hellsten et al. (1998).

The X-ray forest distribution function depends on the Press-Schechter distribution of galaxy clusters, the cluster mass-temperature relationship and the gas distribution inside galaxy clusters (equation (6)). In the following we discuss several important factors which can affect the result.

The key element of the Press-Schechter function is the mass variance, $\sigma(M)$. The present mass variance $\sigma(z = 0, M)$ is calculated from the present power spectrum filtered through a top-hat window, and normalized by the the mass variance at $8h^{-1}$ Mpc, σ_8 . The estimation of σ_8 involves fitting the Press-Schechter function with the observed spatial

number density of local clusters Henry & Arnaud (1991); White et al. (1993); Viana & Liddle (1996, 1999). In this evaluation a crucial relationship is the mass-temperature relationship of equation (3). Although there are both numerical and observational evidences for this relationship, it has a well-known problem of the “recent-formation approximation”: the clusters observed today formed just before we observe them. To resolve this problem two different methods (Lacey & Cole 1993; Sasaki 1994) were proposed to substitute the Press-Schechter function, both of which gave nearly the same result (Viana & Liddle 1996). Based on the merging-halo formalism of Lacey & Cole (1993), Voit & Donahue (1998) derived a new $M_{vir} - T_X$ relation and claimed that equation (3) overestimated temperature evolution and so the numbers of high- z clusters. Their conclusion would affect the X-ray forest distribution function of Fe XXV discussed here, but not O VIII. The reason is that the exponential term of Press-Schechter function will only become crucial at high temperature ($> 10^7\text{K}$), well above the temperature of the ionization peak of O VIII at $\sim 2 \times 10^6\text{K}$. However it would be important to investigate this effect because it would largely decrease the possibility of detecting the highly-ionized heavy metal absorptions lines, such as Fe XXV.

Another important uncertainty which can affect the X-ray distribution function is the metal abundance inside clusters. Using *ASCA*, Mushotzky et al. (1996) shows the mean abundances of O, Si and Fe of four galaxy clusters are 0.48, 0.65 and 0.32 respectively, which are close to the values used in this paper. However, there are a few factors which can affect the metal distribution. First, the metal abundances can depend on the mass of the cluster or group. Recent observations by Hwang et al. (1999) show at temperature above 1 keV, the metal abundances are roughly $0.3 M_\odot$, with little variance, while at temperature below 1 keV, the metal abundances drop very fast (Renzini 1997; Davis, Mulchaey & Mushotsky 1999, and references there in). If it is real, this effect can dramatically drop the possibility of observing Oxygen absorption lines because of its low peak temperature of

ionization. Another factor is the assumption in this paper of constant metal abundances upto redshift as high as $z \sim 3$, although this is important only for the richest systems which have significant column density. No direct evidence shows a constant metal abundances beyond $z \sim 0.3$ (Mushotzky & Loewenstein 1997).

Further progress in this subject relies on both numerical simulations and observations. Large-scale simulations on the X-ray clusters would provide us more accurate information on the X-ray forest distribution. On the observation side, with the launch of *Chandra* and *XMM*, we would expect a few O VII or O VIII absorption lines by observing low and moderate redshift quasars. In the future, *Constellation-X* will provide us superior spectrum of the X-ray forest, with the pioneer of probing the number and distribution of objects in the universe.

We are grateful to Greg Bryan for many useful discussions and helpful suggestion on calculating the power spectrum. We thank Rasalba Perna for kindly discussions on her paper. The code for calculating power spectrum is provided by Daniel Eisenstein and Wayne Hu. We would also like to thank MIT/CXC team for help on using X-ray softwares. We also thank the suggestions from the referee. This work is supported in part by NASA contract NAS 8-38249.

REFERENCES

- Aldcroft, T., Elvis, M., McDowell, J & Fiore, F. 94, ApJ, 437, 584
- Anders, E. & Grevesse, N. 1989, Geochim. Acta, 53, 197
- ASC Science Center 97, AXAF Proposers' Guide
- Basko, M.M., Komberg, B.V. & Moskalenko, E.I. 1981, Soviet Astron. 25 (3), 402
- Bahcall, N.A. & Fan, X. 1998, ApJ, 504, 1
- Bond, J.R., Cole, S., Efstathiou, G. & Kaiser, N. 1991, ApJ, 379, 440
- Bryan, G.L. & Norman, M.L. 1998, ApJ, 495, 80
- Burles, S. & Tytler, D. 1998, ApJ, 499, 699
- Canizares, C.R. & Fang, T. 1998, in "Fundamental Parameters in Cosmology" XXXIII, Rencontres de Moriond.
- Cen, R. & Ostriker, J.P. 1999, ApJ, 514, 1
- Davis, D.S., Mulchaey, J.S. & Mushotsky, R.F. 1999, ApJ, 511, 34
- Eisenstein, D.J. & Hu, W. 1998, ApJ, 498, 137
- Eke, V.R., Cole, S., Frenk, C.S. & Henry, J.P. 1998, MNRAS, 298, 1145
- Eke, V.R., Cole, S. & Frenk, C.S. 1996, MNRAS, 282, 263
- Ettori, S & Fabian, A.C. 1999, MNRAS, 305, 834
- Evrard, A.E., Metzler, C.A. & Navarro, J.F. 1996, ApJ, 467, 489
- Frenk, C.S. et al. 1999, ApJ, 525, 554

- Fukugita, M., Hogan, C.J. & Peebles, J.P.E. 1998, *ApJ*, 503, 518
- Gil’fanov, M.R., Syunyaev, R.A. & Churazov, E.M. 1987, *Soviet Astron. Lett.* 1987, 13 (1), 3
- Hellsten, U., Gnedin, N.Y. & Miralda-Escudé, J. 1998, *ApJ*, 509, 56
- Henry, J.P. & Arnaud, K.A. 1991, *ApJ*, 372, 410
- Hjorth, J., Oukbir, J. & van Kampen, E. 1998, *MNRAS*, 298, L1
- Hwang, U., Mushotzky, R.F., Burns, J.O., Fukazawa, Y. & White, R.A. 1998, *ApJ*, 516, 604
- Krolik, J.R. & Raymond, J.C. 1988, *ApJ*, 335, L39
- Lacey, C. & Cole, S. 1993, *MNRAS*, 262, 627
- Lacey, C. & Cole, S. 1994, *MNRAS*, 271, 676
- Lahav, O., Rees, M.J., Lilje, P.B. & Primack, J.R. 1991, *MNRAS*, 251, 128
- Markevitch, M., 1999, *ApJ*, 522, 13
- Mazzotta, P., Mazzitelli, G., Colafrancesco, S. & Vittorio, N. 1998, *A&AS*, 133, 403
- Møller, P. & Jakobsen, P. 1990, *A&A*, 228, 299
- Mushotzky, R.F., Loewenstein, M., Arnaud, K.A., Tamura, T., Fukazawa, Y., Matsushita, K., Kikuchi, K. & Hatsukade, I. 1996, *ApJ*, 466, 686
- Mushotzky, R.F. & Loewenstein, M. 1997, *ApJ*, 481, 63
- Navarro, J.F., Frenk, C.S. & White, S.D.M., 1995, *MNRAS*, 275, 720
- Nevalainen, J., Markevitch, M. & Forman, W.R., 1999, *ApJ*, 526, 1

- Pen, U. 1998, ApJ, 498, 60
- Perna, P. & Loeb, A. 1998, ApJ, 503, L135
- Press, W.H. & Schechter, P. 1974, ApJ, 187, 425
- Rauch, M., Miralda-Escudé, J., Sargent, W.L.W., Barlow, T.A., Weinberg, D.H., Hernquist, L., Katz, N., Cen, R. & Ostriker, J.P. 1998, ApJ, 489, 1
- Renzini, A. 1997, ApJ, 488, 35
- Rines, K., Forman, W., Pen, U., Jones, C. & Burg, R. 1999, ApJ, 517, 70
- Sasaki, S. 1994, PSAJ, 46, 427
- Sarazin, C.L. 1988, X-ray Emissions from Clusters of Galaxies (Cambridge : Cambridge Univ. Press)
- Sarazin, C.L. 1989, ApJ, 345, 12
- Sarazin, C.L. & Bahcall, J.N. 1977, ApJS, 34, 451
- Shapiro, P.R. & Bahcall, J.N. 1980, ApJ, 241, 1
- Spitzer 1978, Physical Processes in the Interstellar Medium (Princeton : Princeton Univ. Press)
- Tormen, G. 1998, MNRAS, 297, 648
- Verner, D.A., Verner, E.M. & Ferland, G.J. 1996, Atomic Data Nucl. Data Tables, 64, 1
- Viana, P.T.P. & Liddle, A.R. 1996, MNRAS, 281, 323
- Viana, P.T.P. & Liddle, A.R. 1999, MNRAS, 303, 535
- Voit, G.M. & Donahue, M. 1998, ApJ, 500, 111

White, D.A. & Fabian, A.C. 1995, MNRAS, 273, 72

White, S.D.M., Navarro, J.F., Evrard, A.E. & Frenk, C.S. 1993, Nature, 366, 429

Fig. 1.— Ionization fractions for O VIII (solid curve), Si XIV (dashed curve) and Fe XXV (dot-dashed curve).

Fig. 2.— The distribution functions of number of absorbers per redshift and column density for Fe XXV. For each of the three cosmological models, the distribution function vs. column density is given at four different redshifts from top to bottom : $z = 0.0$ (solid line), $z = 1.0$ (dotted line), $z = 2.0$ (dashed line), $z = 3.0$ (dot-dashed line). There is little evolution in the $\Omega_0 < 1$ cosmological models, comparing to a more rapid evolution in the $\Omega_0 = 1$ model.

Fig. 3.— The distribution function for Si XIV. Line symbols are the same as the previous figure. The evolution of $\Omega_0 = 1$ model is still faster than low density models, but is milder than Fe XXV.

Fig. 4.— The distribution function for O VIII. Line symbols are the same as the previous figure.

Fig. 5.— Temperature distribution of galaxy clusters at different redshifts, predicted by the Press-Schechter function. For each of the three cosmological models, temperature distribution are plotted from $z = 0$ to $z = 3$. SCDM shows a rapid evolution at high temperature, compared to OCDM and LCDM.

Fig. 6.— Cumulative column density distribution of average absorption line number upto $z = 3$. Each plot gives the absorption line numbers for one ion under the three cosmological models. O VIII shows more absorption lines. For instance, in the SCDM model, O VIII gives twenty-nine lines with column density over 10^{15}cm^{-2} , compared to five for Si XIV and one for Fe XXV.

Fig. 7.— Cumulative redshift distribution of average absorption line number upto $z = 3$. Each plot shows the absorption line number with column density higher than 10^{15}cm^{-2} under the three cosmological models. In general SCDM shows more rapid evolution.

Fig. 8.— Transmission of Fe XXV under the three cosmological models. The line energy is 6.70 keV and spreads over redshift space from $z = 0$ to $z = 3$.

Fig. 9.— Transmission of Si XIV under the three cosmological models. The line energy is 2.01 keV and spreads over redshift space from $z = 0$ to $z = 3$.

Fig. 10.— Transmission of O VIII under the three cosmological models. The line energy is 0.65 keV and spreads over redshift space from $z = 0$ to $z = 3$.

Fig. 11.— The upper plot is the simulated spectrum, containing three O VIII absorption line at 440.11 eV, 464.82 eV and 468.48 eV, respectively. We fit the simulated spectrum by a simple powerlaw plus the Galactic absorption. The lower plot shows the χ^2 , which clearly indicates three absorption features at the corresponding energy. The four big gaps in the upper plot are due to the instrumental gaps.

Table 1. The Cosmological Models

Model	Ω_0	Ω_R	Ω_Λ	h^a	n^b	σ_8
SCDM	1.0	0.0	0.0	0.7	1.0	0.52
OCDM	0.3	0.7	0.0	0.7	1.0	0.87
LCDM	0.3	0.0	0.7	0.7	1.0	0.93

^aHere we set $H_0 = 70 \text{ km s}^{-1} \text{Mpc}^{-1}$

^bWe choose a scale-invariant power spectrum with index $n = 1$

Table 2. Ion Transition Parameters

Ion	Energy (keV)	Oscillator Strength	Abundance ^a	Solar Abundance ^b
O VIII	0.65	0.416	0.5	8.53×10^{-4}
Si XIV	2.01	0.416	0.5	3.58×10^{-5}
Fe XXV	6.70	0.798	0.3	3.23×10^{-5}

^aRelative to solar abundance Z_\odot .

^bRelative to hydrogen number density.

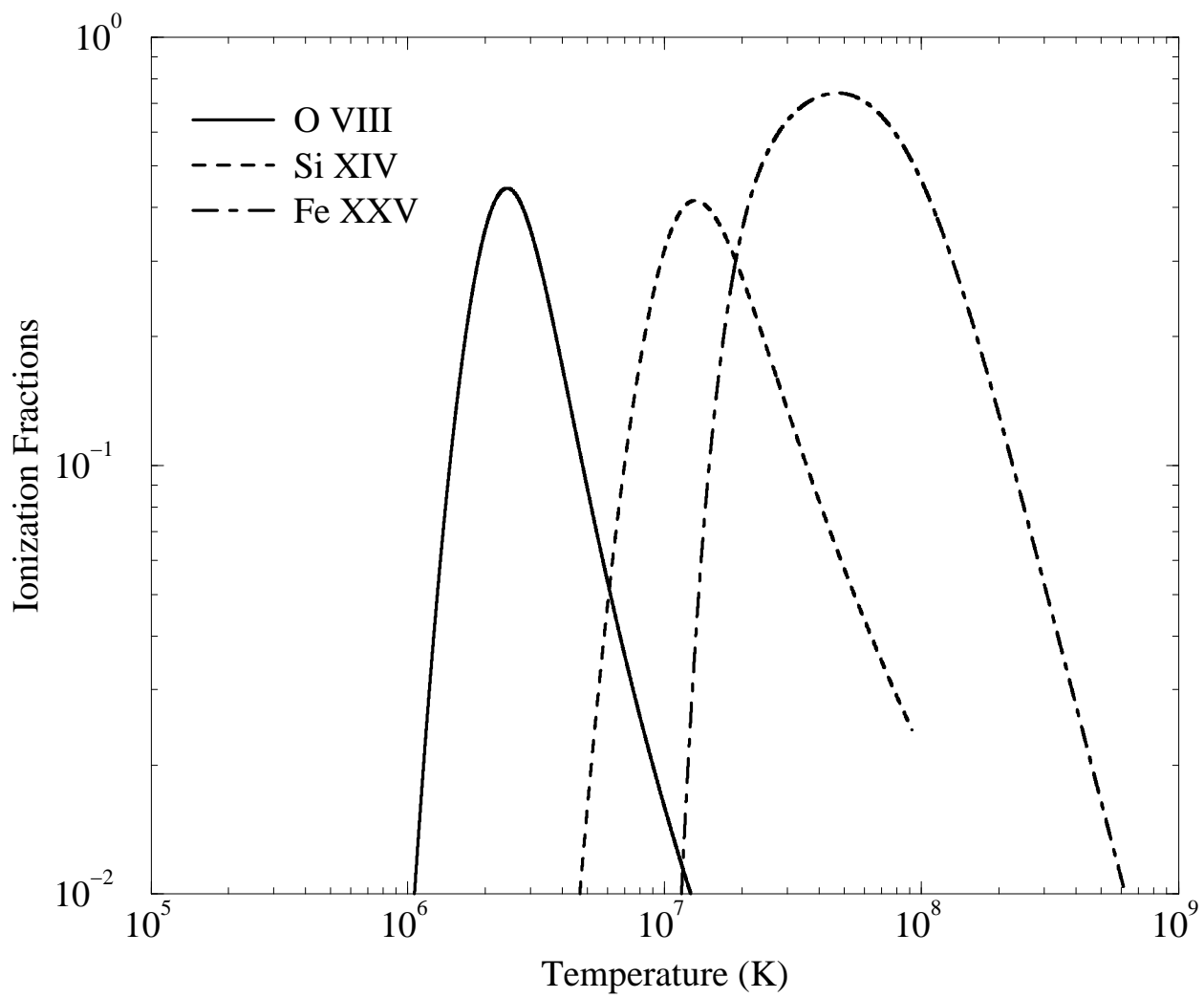
Table 3. Resonant X-ray Absorption Lines at $z = 0.5$

Ion	Instrument	Equivalent Width (eV)	Column Density (cm^{-2})
O VIII	<i>Chandra</i> (LETG)	0.69	$3.5 \cdot 10^{16}$
	<i>XMM</i> (RGS)	0.21	$7.6 \cdot 10^{15}$
	<i>Constellation X</i> (Gratings)	0.04	$1.3 \cdot 10^{15}$
Si XIV	<i>Chandra</i> (MEG)	1.34	$4.7 \cdot 10^{16}$
	<i>XMM</i> (RGS)	2.25	$1.1 \cdot 10^{17}$
	<i>Constellation X</i> (Calorimeter)	0.09	$3.1 \cdot 10^{15}$
Fe XXV	<i>Chandra</i> (HEG)	24.7	$1.7 \cdot 10^{20}$
	<i>XMM</i> (RGS)	N/A ^a	N/A ^a
	<i>Constellation X</i> (Calorimeter)	0.52	$9.2 \cdot 10^{15}$

^aThe energy range of XMM RGS is $0.35 - 2.5 \text{ keV}$

Table 4. Selected O VIII Absorption Lines for XMM Simulation

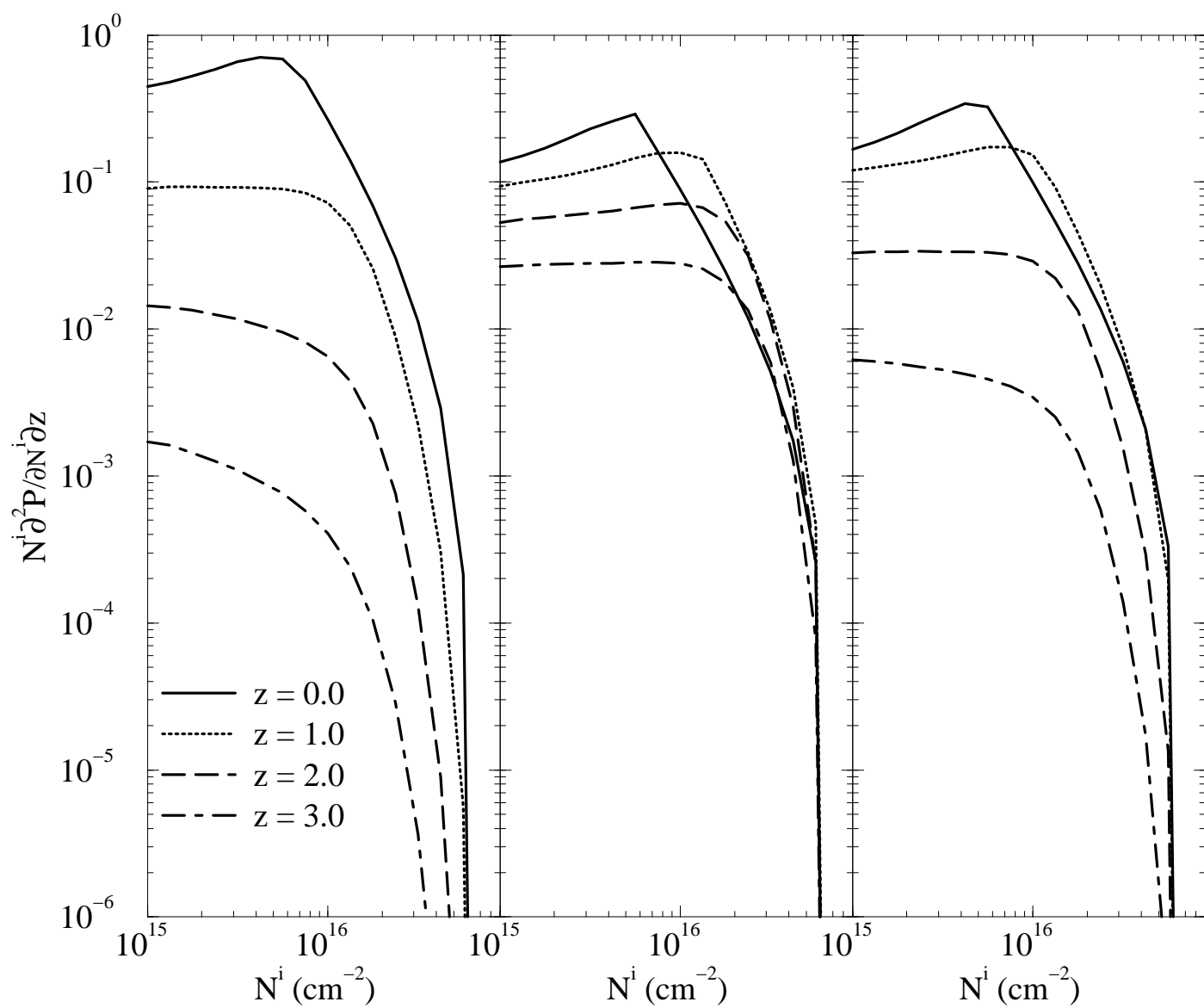
line number	Column Density (cm^{-2})	Redshift	Energy (eV)	Equivalent Width (eV)
1	$4.28 \cdot 10^{16}$	0.486	440.11	0.54
2	$2.80 \cdot 10^{16}$	0.396	468.48	0.80
3	$3.27 \cdot 10^{16}$	0.407	464.82	0.79



SCDM

OCDM

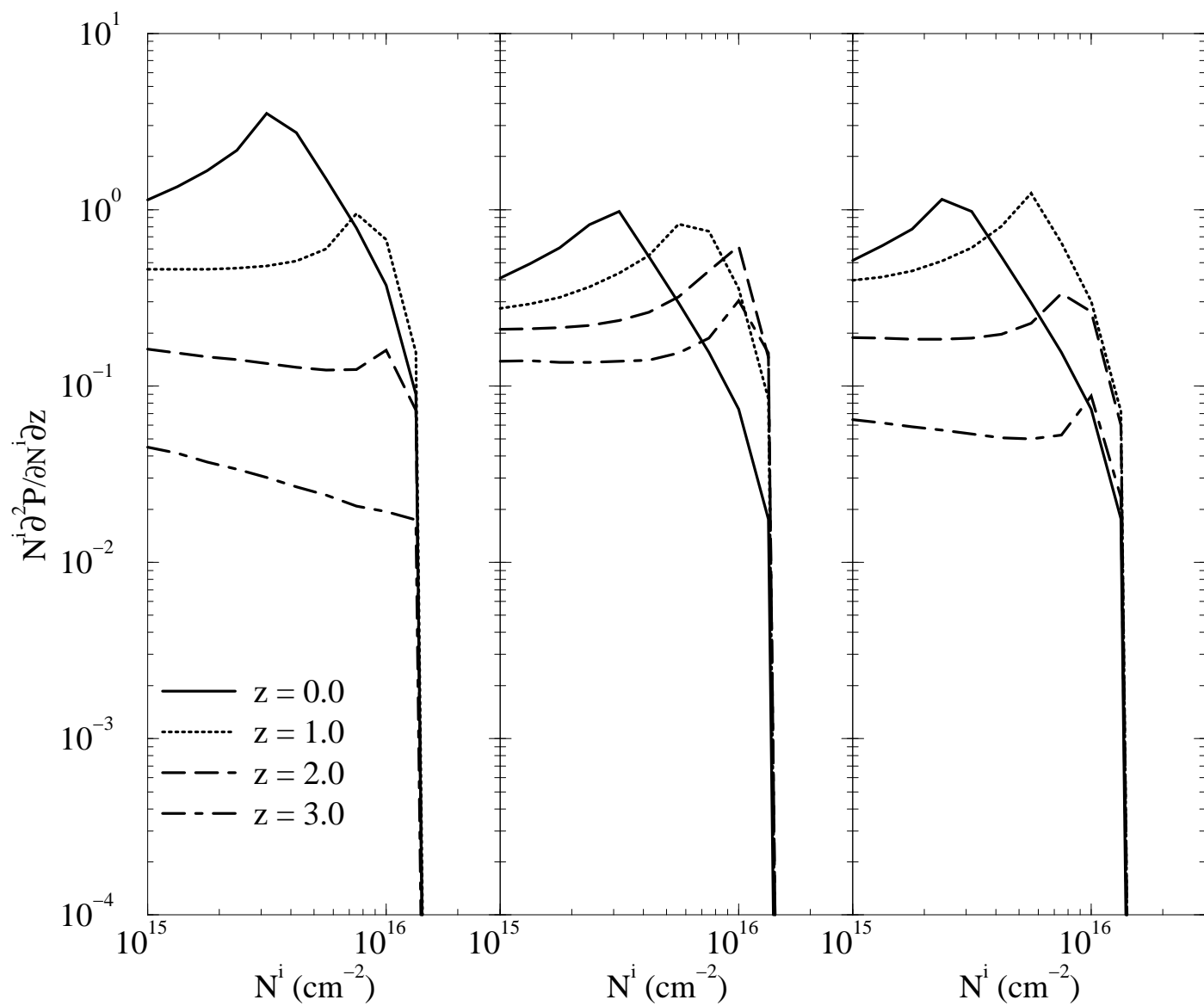
LCDM



SCDM

OCDM

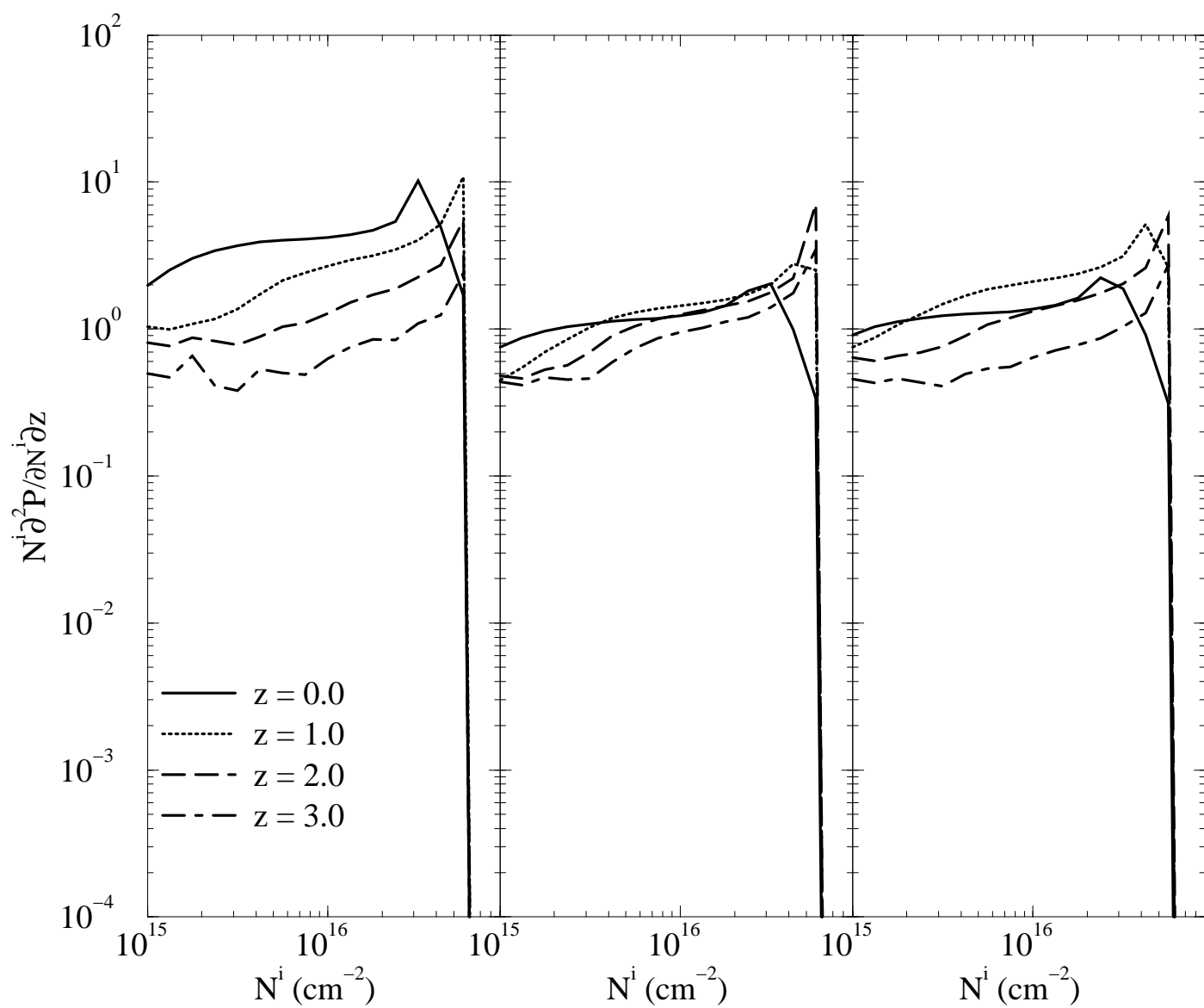
LCDM



SCDM

OCDM

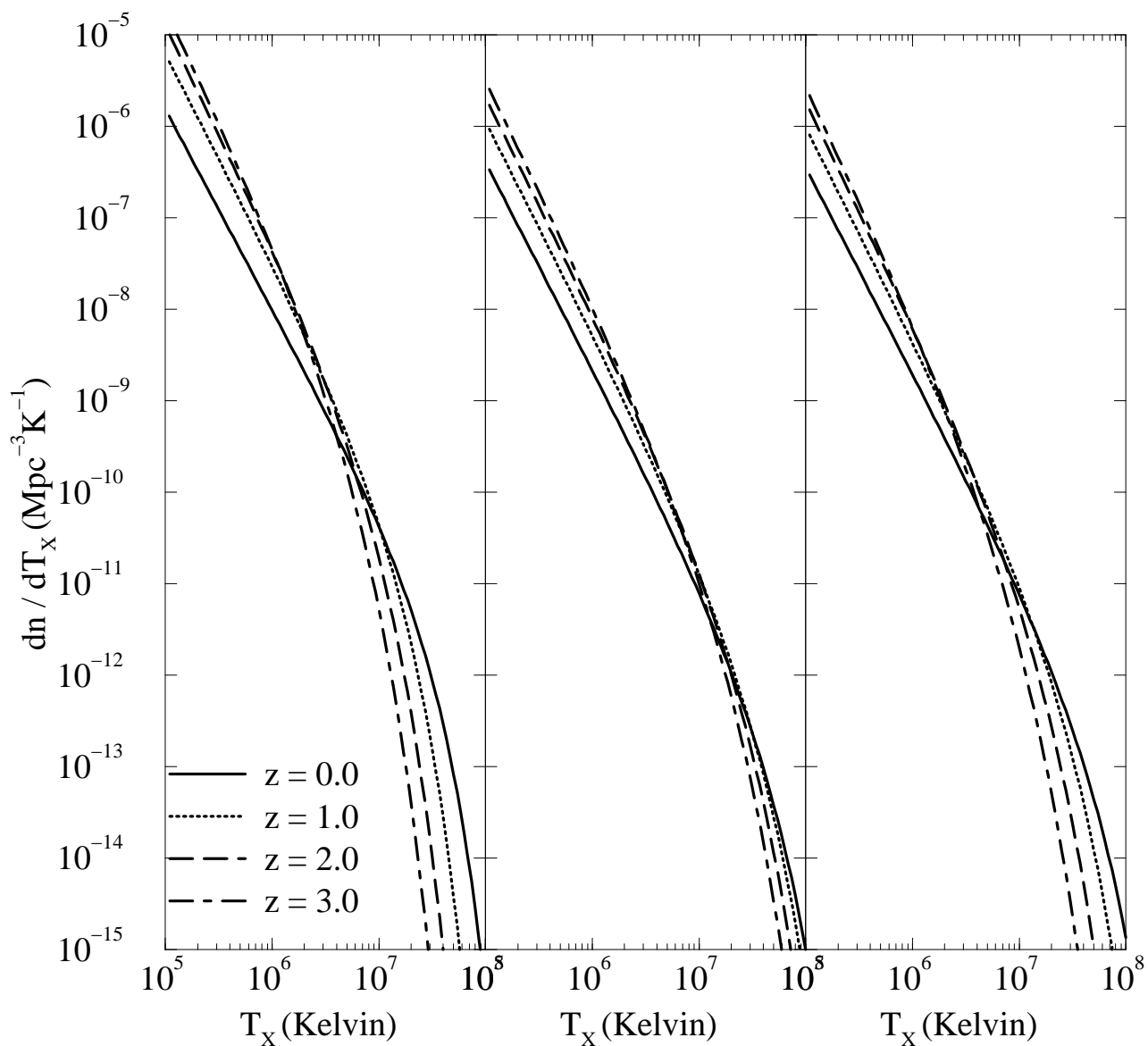
ΛCDM



SCDM

OCDM

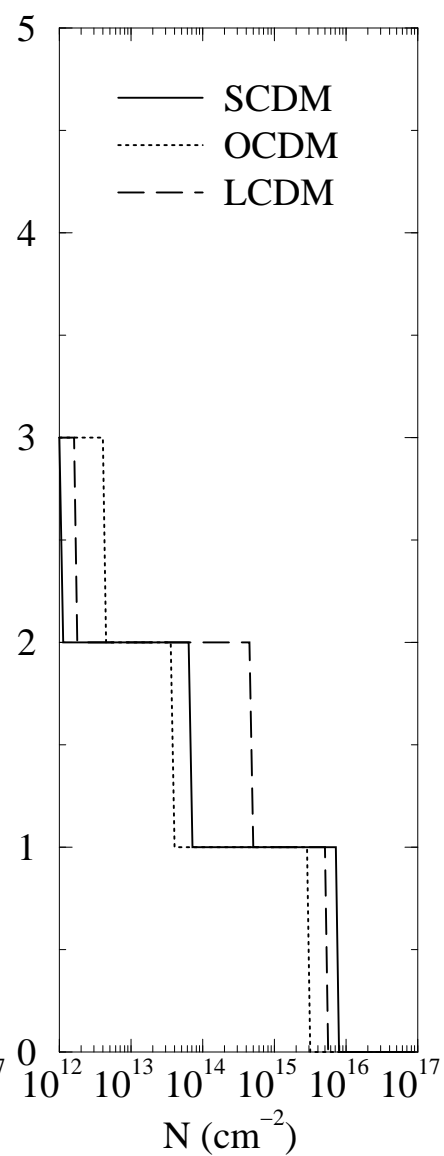
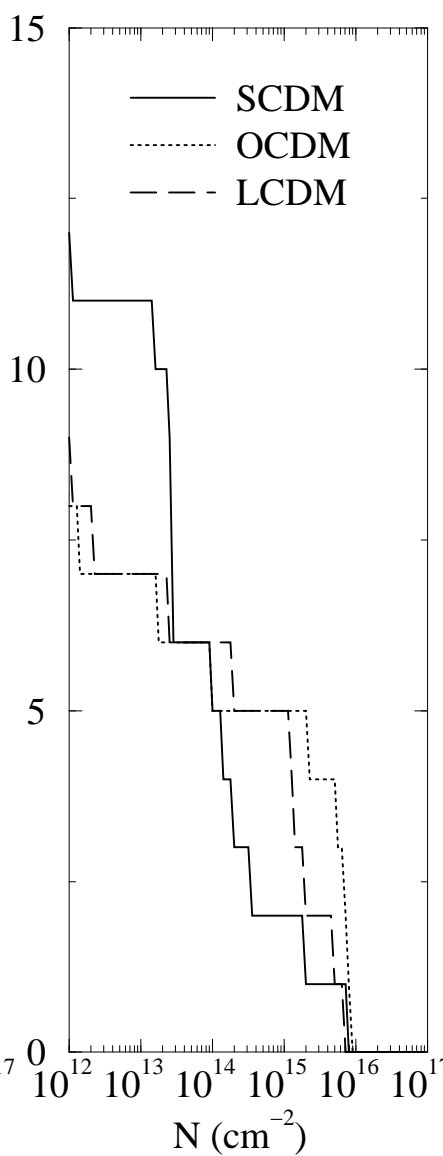
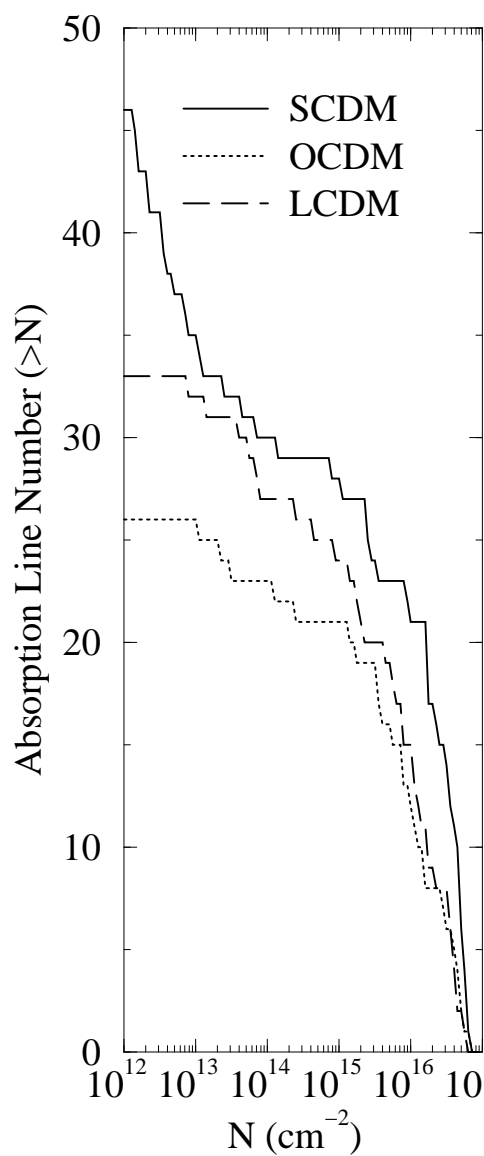
ΛCDM



O VIII

Si XIV

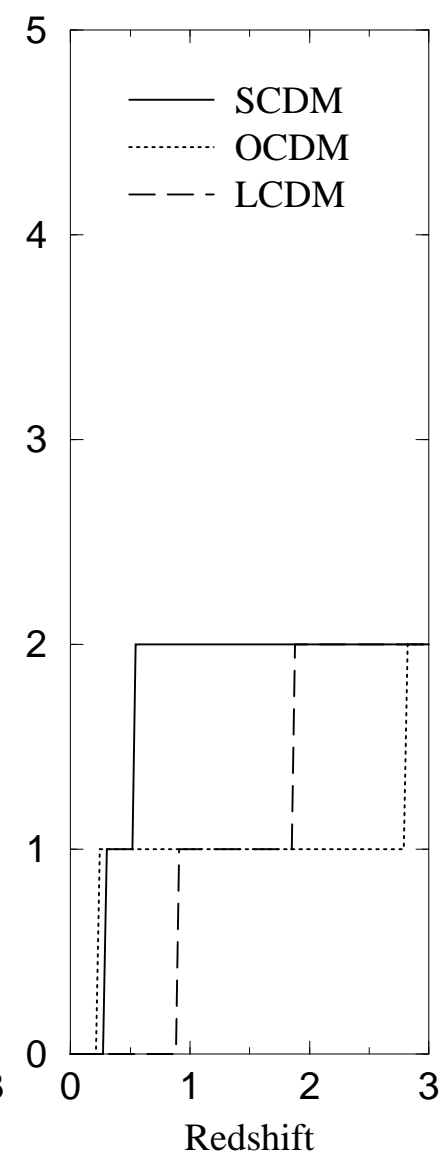
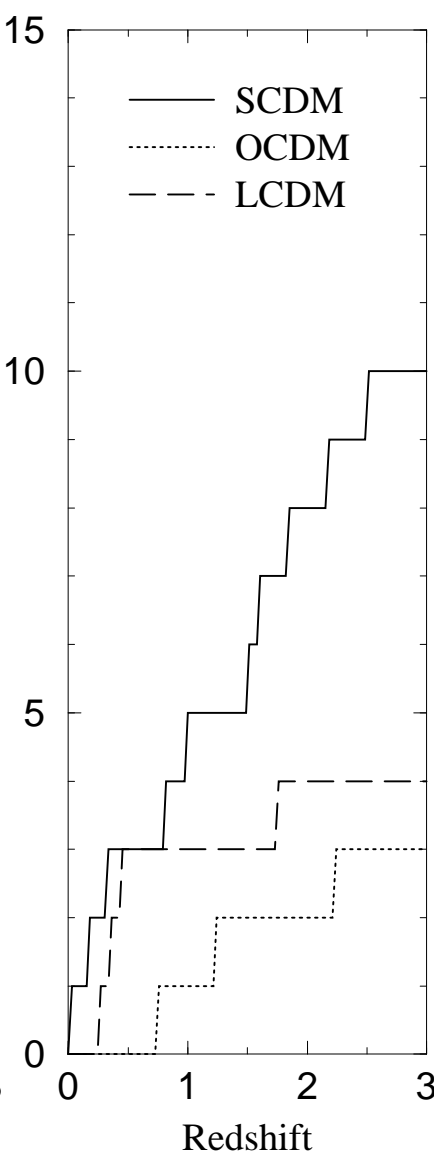
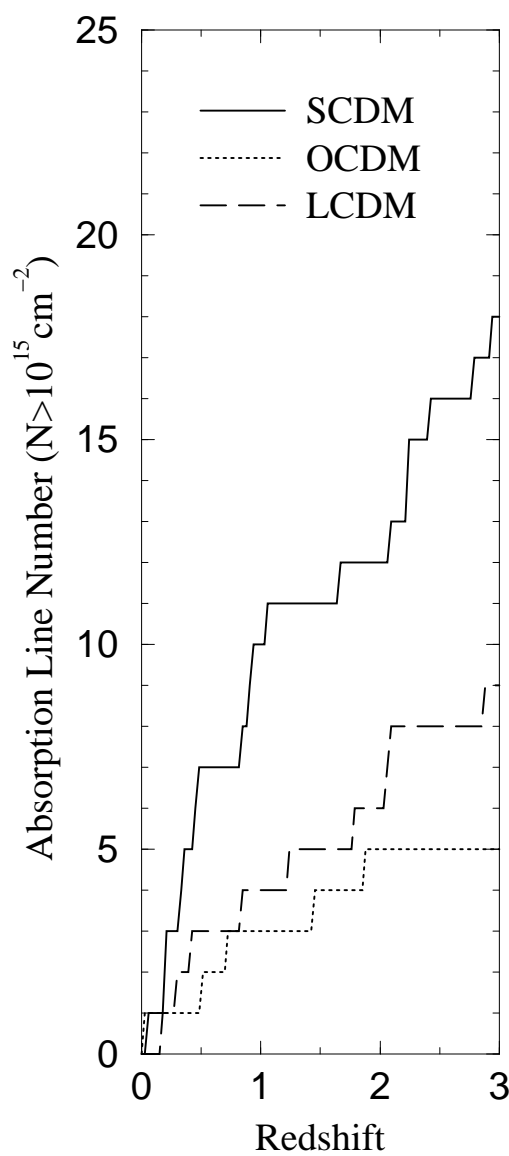
Fe XXV



O VIII

Si XIV

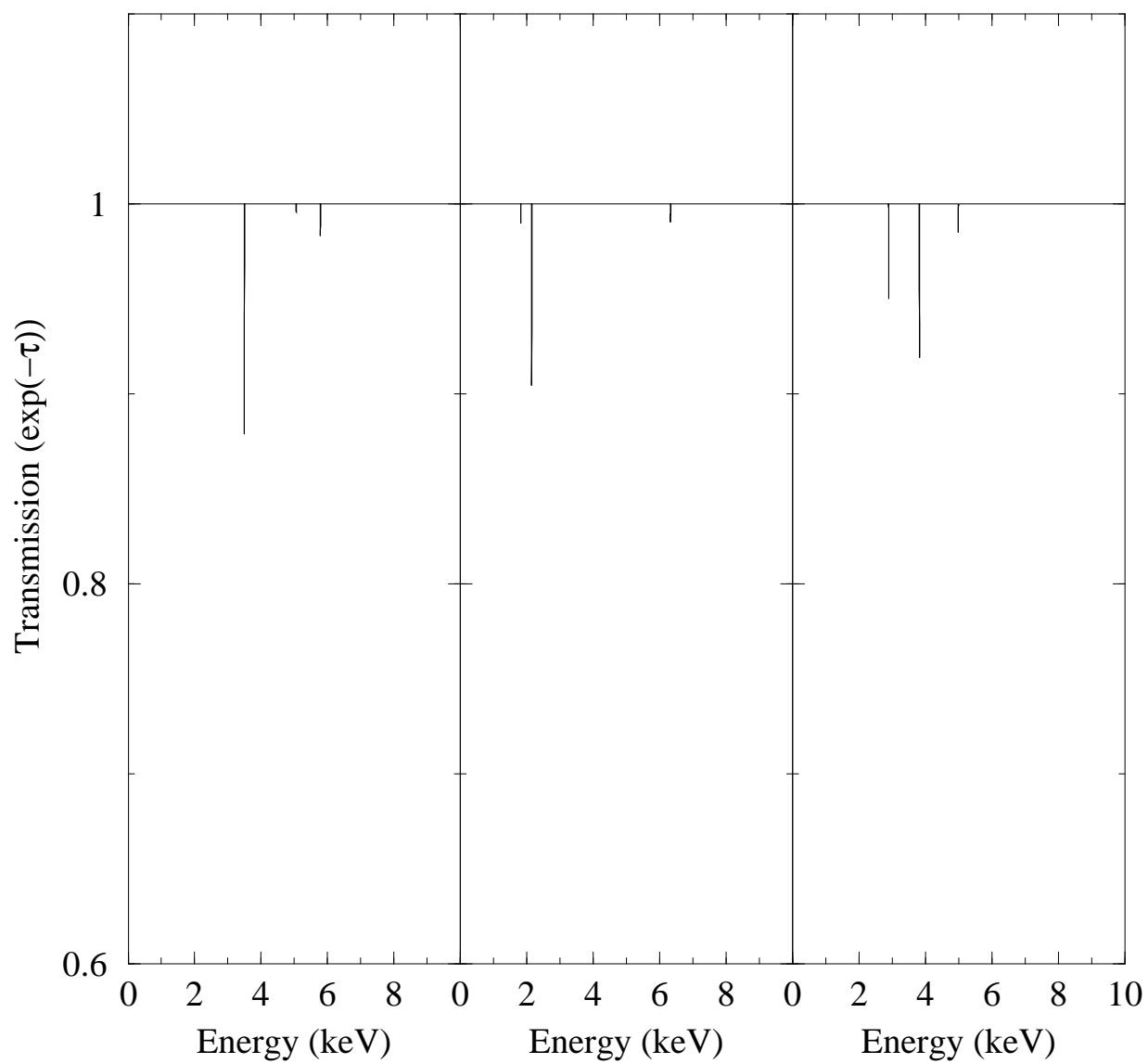
Fe XXV



SCDM

OCDM

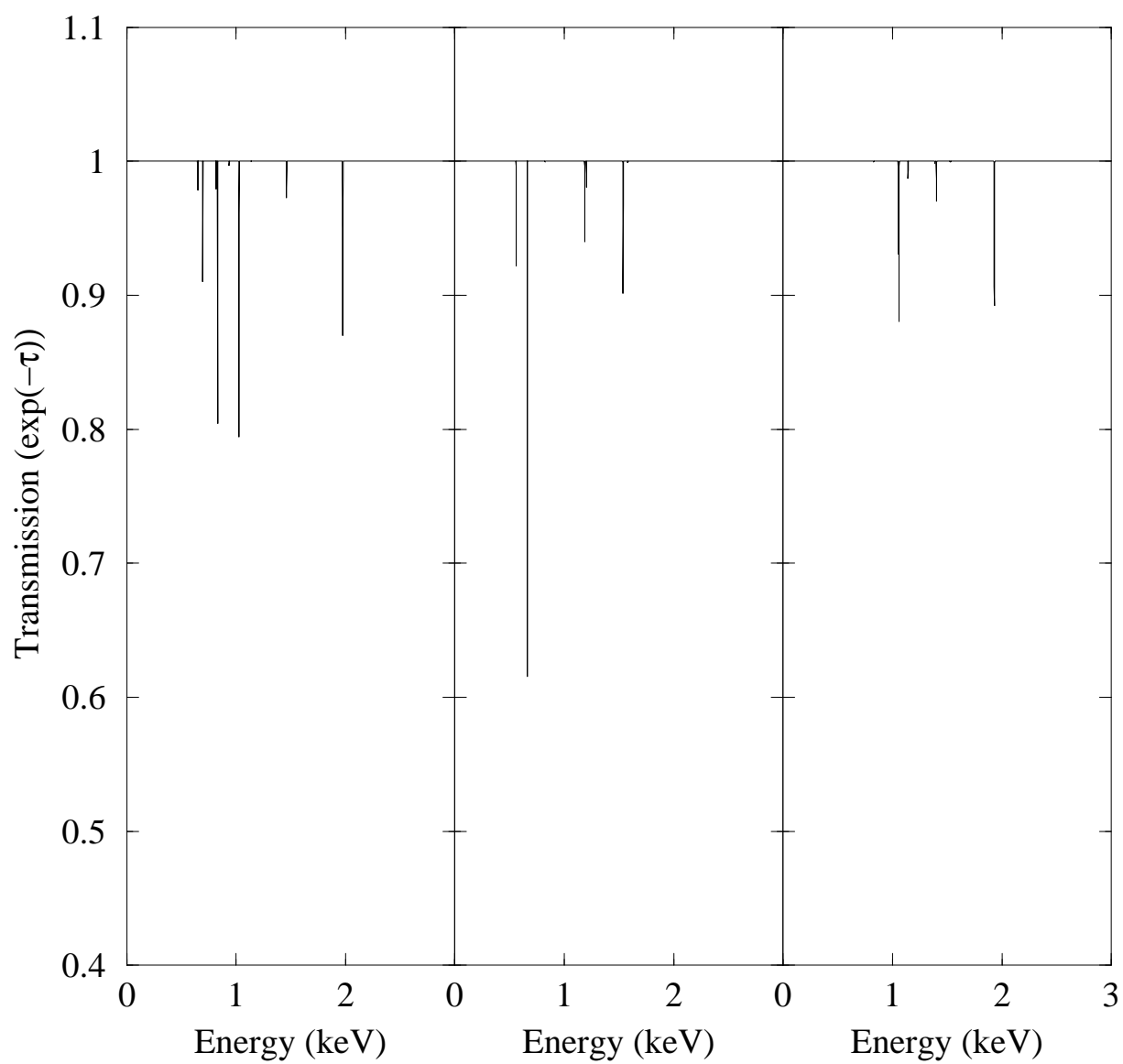
ΛCDM



SCDM

OCDM

ΛCDM



SCDM

OCDM

LCDM

